Observation and Numerical Simulation of Cloud Physical Processes Associated with Torrential Rain of the Meiyu Front

WANG Pengyun* (王鹏云) and YANG Jing (杨 静)

Chinese Academy of Meteorological Sciences, Beijing 100081

(Received November 18, 2001; revised October 19, 2002)

ABSTRACT

Cloud micro-physical structures in a precipitation system associated with the Meiyu front are observed using the balloon-borne Precipitation Particle Image Sensor at Baoshan observatory station, Shanghai during June and July 1999. The vertical distributions of various cloud particle size, number density, and mass density are retrieved from the observations. Analyses of observations show that ice-phase particles (ice crystals, graupel, snowflakes, and frozen drops) often exist in the cloud of torrential rain associated with the Meiyu front. Among the various particles, ice crystals and graupel are the most numerous, but graupel and snow have the highest mass density. Ice-phase particles coexist with liquid water droplets near the 0°C level. The graupel is similarly distributed with height as the ice crystals. Raindrops below the 0°C level are mainly from melted grauple, snowflakes and frozen drops. They may further grow larger by coalescence with smaller ones as they fall from the cloud base. Numerical simulations using the non-hydrostatic meso-scale model MM5 with the Reisner graupel explicit moisture scheme confirm the main observational results. Rain water at the lower level is mainly generated from the melting of snow and graupel falling from the upper level where snow and graupel are generated and grown from collection with cloud and rain water. Thus the mixed-phase cloud process, in which ice phase coexists and interacts with liquid phase (cloud and rain drops), plays the most important role in the formation and development of heavy convective rainfall in the Meiyu frontal system.

Key words: videosonde, cloud micro-physical structure, Meiyu front precipitation, meso-scale numerical simulation

1. Introduction

A rainband often exists along the middle and lower reaches of the Yangtze River in June and July, which produces steady moderate to heavy rainfall called Meiyu rain. The Meiyu rainband is located at the north edge of the subtropical high, produced by the confluence between polar continental air mass from the north and warm monsoon air mass from the south to the west of 130°E, and the colder polar oceanic air mass from the north and tropical air mass from the south to the east of 130°E. Since Meiyu maintains a long period and produces heavy, even torrential rainfall, many studies have been done on the structures and evolution, and mechanisms for its formation. These studies, however, are mostly concerned with synoptic climatology and thermodynamics including coexistence of the high-level jet and low-level jet; interaction between synoptic scale and sub-synoptic scale phenomena; transfer of energy; instabilities; and diagnostic analysis of potential vorticity and radiation cooling, etc.(e.g., Yu and Lu, 1988; Chen, 1989; Xue et al., 1996; Li et al., 2001). Recently some observations from field experiments and numerical simulations explored the structure and evolution of physical parameters, e.g. rainfall, wind field, heat transition, and potential vorticity, etc., associated with the Meiyu front (e.g., Xu et al., 2000; Cheng et al., 2001; Zhai and Gao, 1996).

Rainfall is produced through cloud physical processes which are associated with certain favorable dynamic and thermodynamic conditions. The cloud physical processes also feedback and affect the thermodynamic process through latent heat release associated with the phase transfer among the hydrometeors, and the dynamic process through dragging of falling particles. Therefore, study of the cloud physical pro-

*E-mail: wangpy@cams.cma.gov.cn

cesses and their interaction with dynamic and thermodynamic processes is an important part in understanding the mechanism for formation and evolution of mesoscale heavy rain. There are probably two ways to study the cloud physical processes in a heavy rainfall system. One is observation and analysis either through research aircraft flying directly in the cloud and sampling the microphysical parameters or remote sensing using radar and satellite. The other is numerical model simulations. The problem and limitation of aircraft observation is that the aircraft can hardly fly into strong developing convective cloud, which however, may be the most important part for producing heavy rainfall, and in general the aircraft only fly through cloud on several levels but do not get the continuous vertical distribution of the cloud physical structure. Obviously remote sensing observations using radar and satellite are an indirect way and cannot get information in detail. Some numerical studies have shown the interaction between cloud physical processes and synoptic systems (e.g. Reisner et al., 1998). However, few observational data on the cloud physical structure are available for verifying the simulations.

The heaviest rainfall of the Meiyu front in the last recent 100 years happened in June and July 1999 in the middle and lower reaches of the Yangtze River. The total rainfall in June reached 300–500 mm, even reaching up to 570–870 mm at the eastern part in the South of Yangtze River, an amount which was 2–3 times the normal yearly rainfall. Monthly rainfall at Shanghai, Anqing, Suzhou, and Hangzhou, etc. in June reached their highest records since the founding of P. R. China in 1949. The rainfall at Longhua observational station of Shanghai was 726 mm in June, which was the highest record at the station since the meteorological record began in 1873. The period from 22 June to 1 July was the heaviest and longest-lasting rainfall period in the month. For studying the cloud physical processes in the Meiyu frontal system, a balloon-borne video-sounding system, Precipitation Particle Image Sensor (Takahashi et al., 1995), was used to directly observe the cloud micro-physical structures vertically from the base to the top of the cloud during this period at Baoshan observational station of Shanghai. The observations include cloud particle phase, size, concentration, and electric charging. A WSR–88D Doppler radar at Shanghai was operated to support recording the location and intensity of the heavy rain and its evolution. A total of 14 video soundings were launched into six heavy rainfall clusters. Also, for comparison with the observations, a numerical simulation was done using the non-hydrostatic mesoscale model MM5. This paper will present the main results from both observation and simulation.

2. Observation of cloud micro-physical structures using the videosonde system

2.1 *PPIS*

The Precipitation Particle Image Sensor (PPIS) is a balloon-borne videosonde from which images of precipitation particles are recorded by a camera (Takahashi et al., 1995). An infra-red light is set in the videosonde such that its beam is 15 mm above and parallel to the line of the camera. Interruption of the infra-red beam by a precipitation particle larger than 0.5 mm in diameter triggers a flash lamp just above the camera lens. The flash lamp has a pulse duration of 1/22000 s and can be triggered up to twice per second. Image signals are converted to a frequency between 10 Hz and 1 MHz and sent to the ground by a 1680–MHz carrier wave. In addition to the particle images, the PPIS also records the electric charge on the particles and the ambient temperature, humidity, and pressure. The data are transmitted to the ground station where they are displayed on a TV screen and recorded on a video tape for review and analysis. Particles (ice crystals, graupel, snowflakes, raindrops, and frozen drops) are distinguished from each other by differences in shape, transparency, and air bubbles.

2.2 *Observations*

During the period of 24–30 June 1999, three cold air masses passed over and affected China from the northwest to the southeast. Led by the positive vorticity advection ahead of the trough, three Southwest vortexes moved eastward and developed into the Jianghui cyclones. Associated with the eastward moving of the southwest vortex, the low level jet was strengthened, supplying abundant moisture for precipitation. Eastward moving cloud clusters associated with the low vortex along the Meiyu front were seen on the GMS infrared satellite cloud picture. Hence heavy rainfall was produced in Shanghai area. The daily rainfall amounts at Baoshan station from 24 to 30 June were 65.8 mm, 32.1 mm, 42.5 mm, 23.7 mm, 31.9 mm, 1.7 mm, and 151.7 mm, respectively. A total of 14 videosondes were launched during this period.

On 24 June, two videosondes, UP11 and MIX10, were launched at 0700 and 0930 BT (Beijing time, here and Following) when the rain intensity was 7.1 mm h^{-1} and 5.5 mm h^{-1} (Fig. 1a). On 26 June, two videosondes, UP9 and MIX5, were launched at 0440 and 1611 when the rain intensity was 3.3 mm h^{-1} and 3.2 mm h^{-1} (Fig. 1b). The balloons carrying the sonde system did not drift too far away since the wind was not strong. The following will give the results of these four sondes.

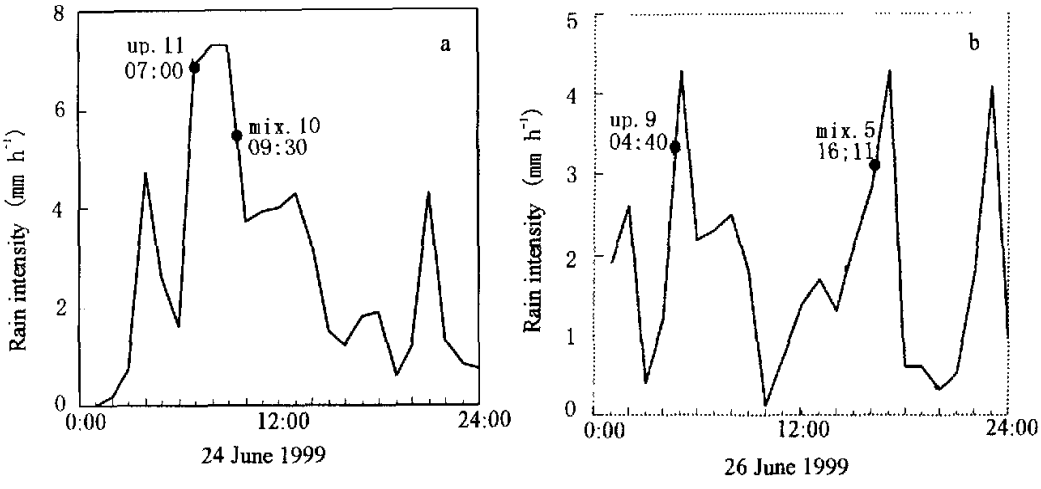

Fig. 1. Rainfall intensity and videosonde launching. (a) 24 June 1999; (b) 26 June 1999.

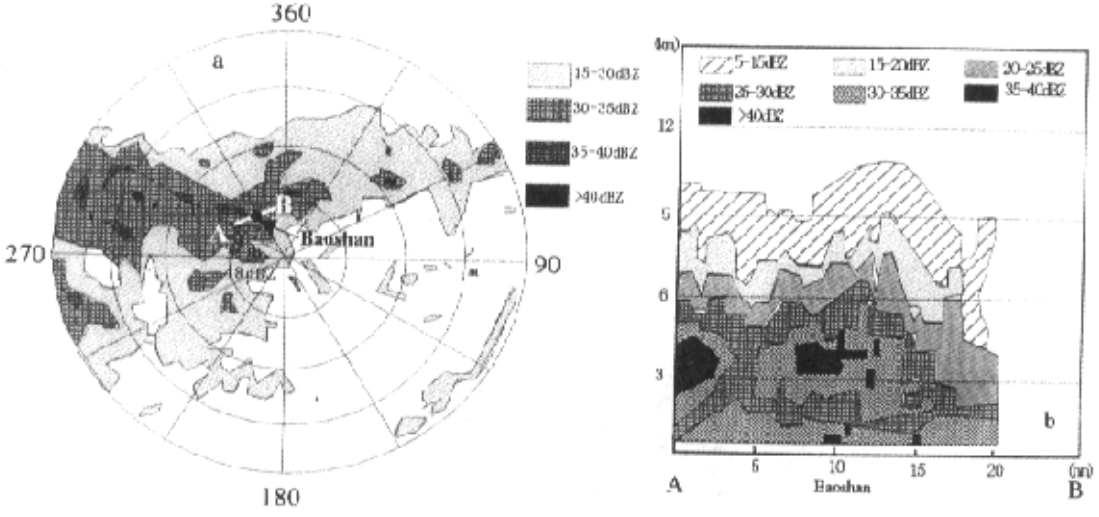

Fig. 2. WSR-88 radar reflectivity. (a) PPI at 0700 BT 24 June 1999. (b) RHI from point A (azimuth 301° and 31 nmi) to B (339° and 28 nmi). Baoshan was located at 10 nmi.

2.2.1 *UP11*

Videosonde UP11 was launched at 0700 BT 24 June. The radar PPI echo showed strong convective cells embedded in a wide rain band (Fig. 2a). The intensity of the echo was 48 dBz at observation site Baoshan, which is located at 320° azimuth and 28 nautical miles from WSR88D radar at Shanghai. The vertical cross section along the line from point A (301° azimuth and 31 nautical miles from the radar) to point B (339° azimuth and 28 nautical miles from the radar) showed the echo top was 10 km high over Baoshan (Fig. 2b). GMS satellite infrared cloud cover at 0730 showed convective cloud was well developed and the cloud top reached to 11.94 km where the temperature was -45.5°C over Baoshan. The rain intensity was 7.1-7.5 mm h^{-1} during 0700-0900 (Fig. 1a).

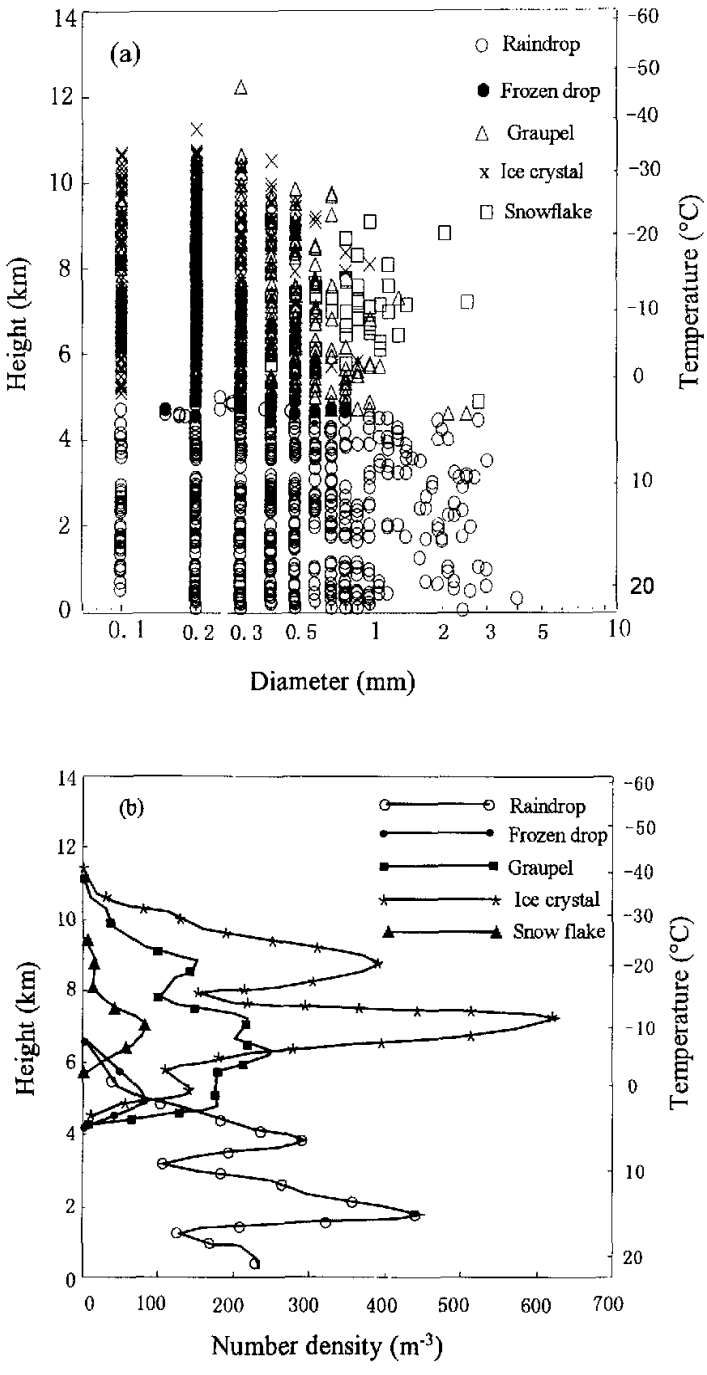

Fig. 3. UP11 observation. (a) Size – height distribution. (b) Number density — height distribution. (c) Mass density — height distribution.

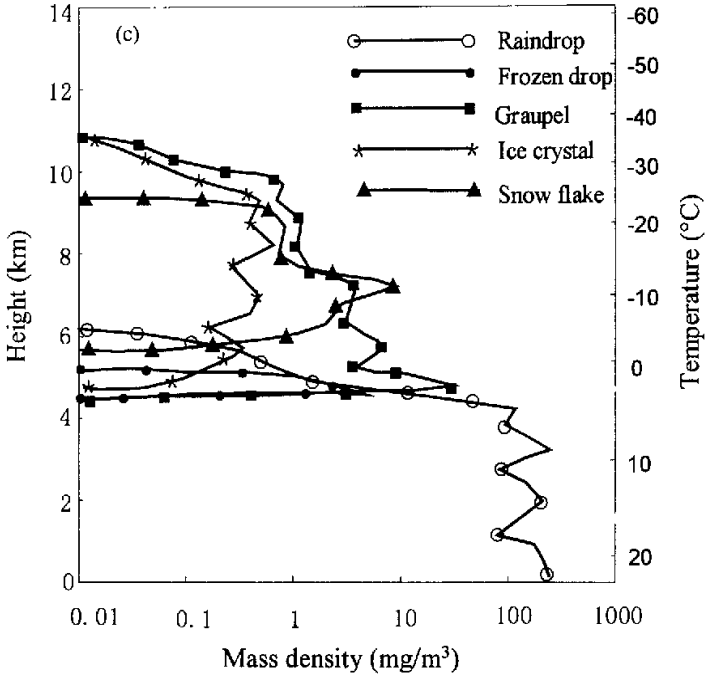

Fig. 3. (Continued)

UP11 discovered a total of 1475 particles among which most were small ice crystals with diameters less than 1 mm. Graupel, with diameters of 0.5–2.5 mm, were vertically distributed from 4.5 km in height to the cloud top. Some frozen drops existed near the 0°C level. Below the 0°C level, there were still some larger un-melted graupel and snowflakes. The largest graupel, with a diameter of 2.5 mm, was observed at the 3°C level, which was the remenant of a larger particle falling from above and melting (Fig. 3a).

The number density distributions for various particles were calculated for every 500 m height interval. The sample volume was estimated by subtracting the volume while the flash was recharging (0.6 s), $V = S(H - 0.6WN)$, where $S = 0.02 \times 0.029$ m^2 is the horizontal cross section of the camera view, H=500 m is the height interval for calculation, W is the sonde lifting velocity, and N is the total number of flashes during the 500 m height interval. The number density distribution (Fig. 3b) shows ice crystals, with an average number of 300–400 m^{-3}, were the most plentiful, concentrating from 6 km to 10 km in height with a maximum of 610 m^{-3} at 7 km (near the −10°C level). The graupel distribution was similar to, but fewer than, that of ice crystals, with a maximum of 250 m^{-3}. Snowflakes had the smallest number density of only tens per cubic meter. Frozen drops were distributed from 4 km to 6 km with a peak value of 81 m^3 at 5 km (near the 0°C level). Some super-cooled raindrops coexisted with the ice-phase particles above the 0°C level from 5 km to 6 km.

The mass density was calculated supposing the density of raindrops was 1 g cm^{-3}, frozen drops 0.9 g cm^{-3}, graupel 0.3 g cm^{-3}, ice crystals and snow 0.1 g cm^{-3} (Takahashi et al. 1995). Among the various particles in the cloud, graupel had the highest mass density. Comparing with the number density distribution, the mass density of the graupel was increasing with decreasing height, reaching its maximum of 25.6 mg m^{-3} at 4.8 km (~ 2°C). Snowflakes were the next highest mass density, with a maximum of 8.8 mg m^{-3} at the −10°C level. Ice crystals had the smallest mass density, less than 1 mg m^{-3} in average. In the same way as for graupel, the mass density distribution of ice crystals was different from its number density distribution, but nearly equally distributed with height. Frozen drops were mostly concentrated near the 0 °C level with a maximum of 8.1 mg m^{-3} (Fig. 3c).

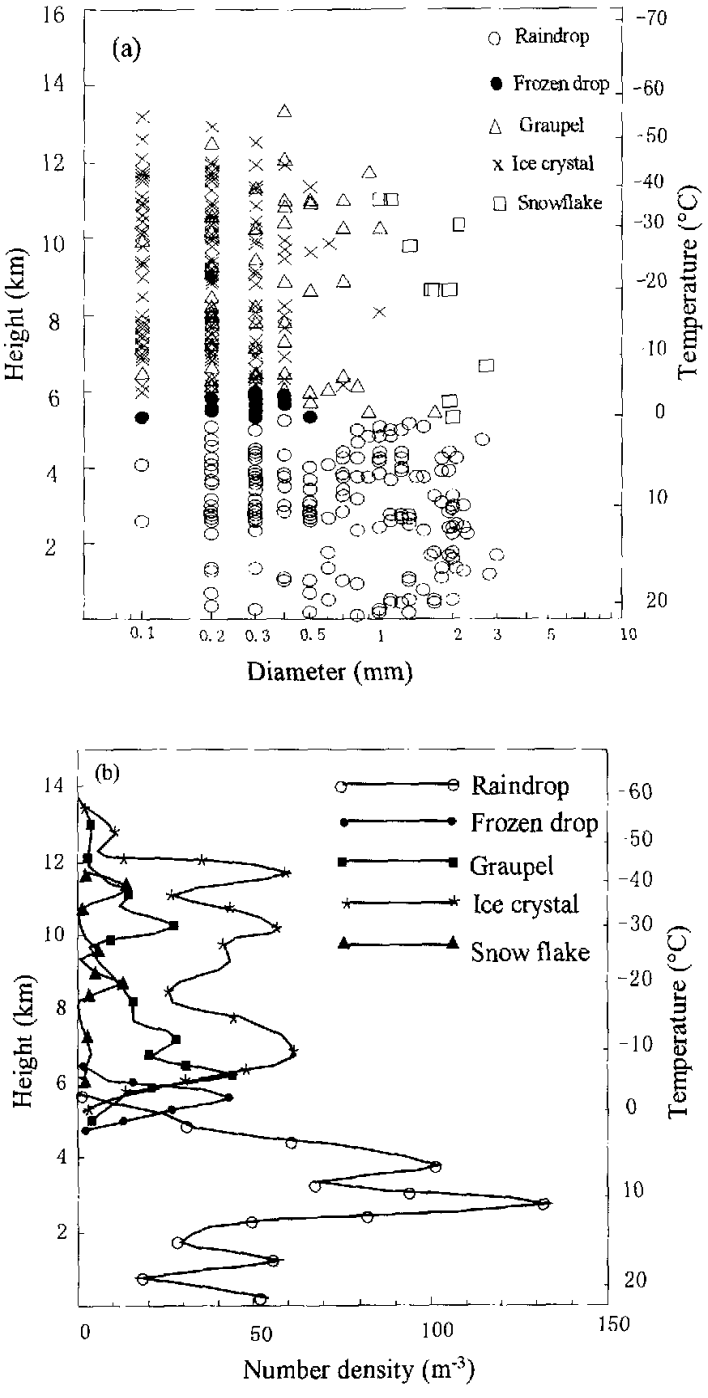

Fig. 4. Same as Fig. 3 but for MIX 10.

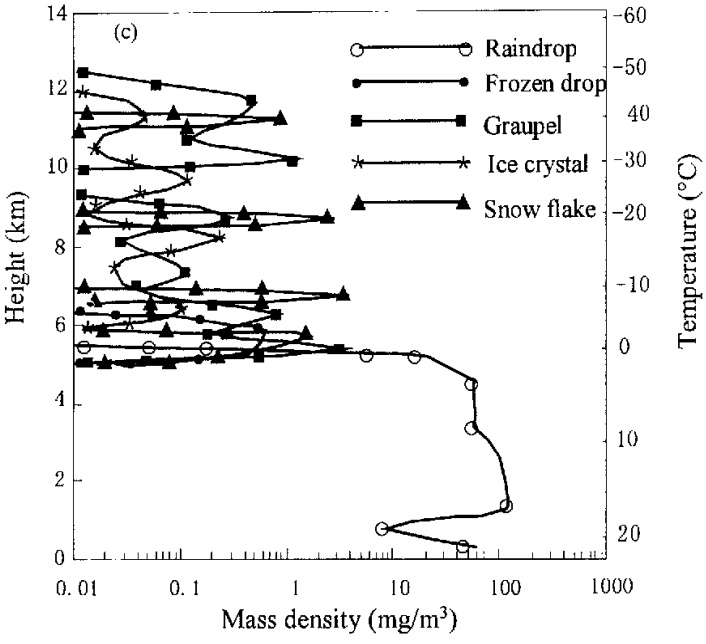

Fig. 4. (Continued)

2.2.2 *MIX10*

Following UP11, MIX10 was launched at 0930 when the rain intensity decreased to 5.5 mm h^{-1} (Fig. 1a). This videosonde system (and MIX5, to be discussed later) included both infrared and micro scanning so the form of particles can be seen more clearly. The sonde discovered 446 particles with the maximum diameter of 3 mm. Similar to UP11, ice crystals were the most plentiful and were observed in wide height levels, from 6 km up to 13 km. Their diameters were mostly in the range 0.1 0.4 mm and the maximum was 1 mm observed at 8 km (−16°C). Frozen drops, with a maximum diameter of 0.5 mm, appeared at the 5.3–6 km level where temperature was 0°C– −5°C. Graupel was also widely spread, from the 0°C level up to the cloud top, but mostly concentrated near 6 km and 10 km. Most graupel diameters were 0.5–0.9 mm; the largest one (1.7 mm) was observed at the −4°C level. Snowflakes, with diameters of 1 mm to 3 mm, were separately distributed at several levels (Fig. 4a).

The distribution of particle number density for MIX 10 (Fig. 4b) shows ice crystals had the highest number density with a the maximum of 60 m^{-3} at −8°C, and 50 m^{-3} at −30°C and −45°C. Graupel had a similar distribution but with a maximum of 44 m^{-3} at −5°C. The peak value of snowflakes was 15.6 m^{-3} at −40°C. The maximum of frozen drops was 45 m^{-3} at −2°C.

The mass density distribution is shown in Fig. 4c. Comparing Fig. 4c carefully with Fig. 4b, we can see that the higher value of mass density for ice crystals was located at a lower level than that of the higher number density, for example, 0.12 mg m^{-3} at 9.5 km corresponding to 50 m^{-3} at 10.5 km, 0.23 mg m^{-3} at 8 km corresponding to 50 m^{-3} at 10 km, and 0.12 mg m^{-3} at 6 km corresponding to 60 m^{-3} at 7 km, respectively. The mass density of graupel was one order larger than ice crystals, but increasing with decreasing heiht and reaching their peak value of 3.45 mg m^{-3} near the 0°C level. Snowflakes also had a larger mass density but separately distributed in height with a maximum of 4.2 mg m^{-3} at −9°C. The mass density of raindrops under the cloud base was somewhat increasing with decreasing height.

2.2.3 *UP9*

UP9 was launched at 0440 26 June when the cloud top from satellite data was measured at 11.8 km at a temperature of −44.6°C. The radar echo intensity at Baoshan was 35 dBZ. A total of 518 particles were observed. Ice crystals with diameters of 0.2 1 mm and

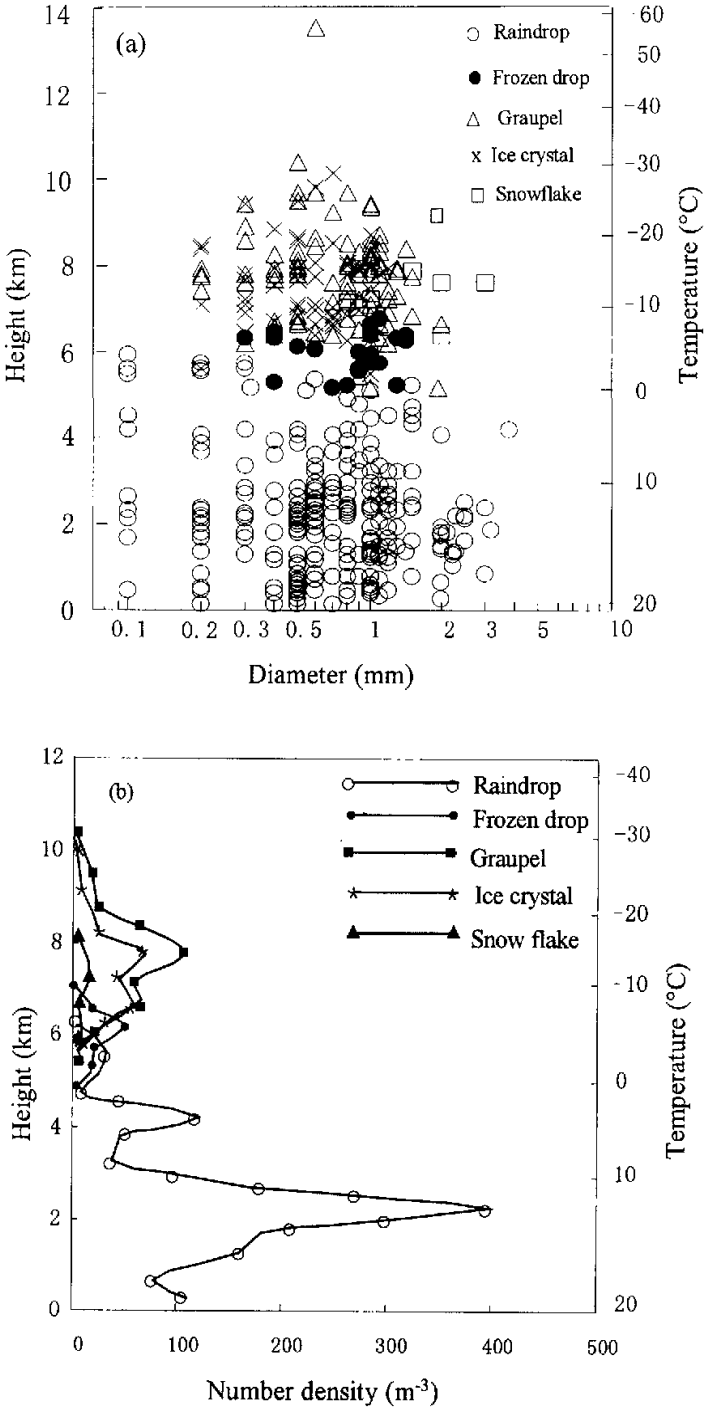

Fig. 5. Same as Fig. 3 but for UP 9.

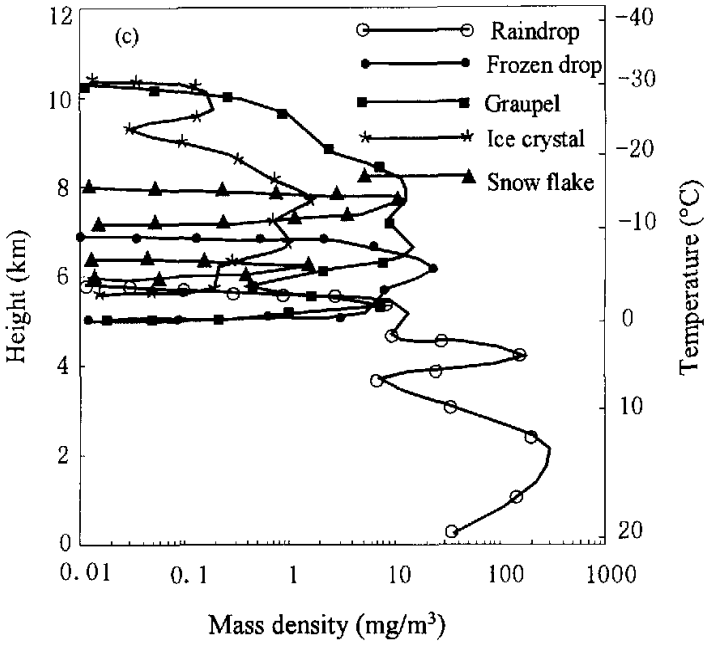

Fig. 5.(Continued)

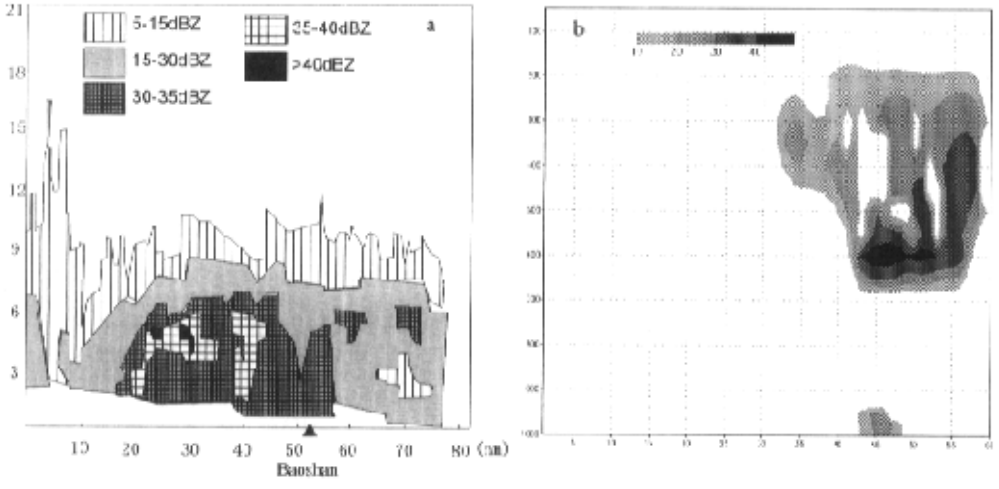

Fig. 6. Radar reflectivity vertical cross section. (a) Observation at 1600 BT 26 June. (b) Model simulation integrated at 33 h valid for 1700 BT 26 June.

graupel with diameters of 0.4 1.6 mm spread from 5.5–10.5 km; frozen drops with diameters of 0.3–1.5 mm mainly existed from 5.1–6.4 km where the temperature was 0°C– -6°C. Above the 0°C level, from 5 km to 6 km, there were some super-cooled raindrops (Fig. 5a).

The number density of graupel was the largest in this case, with peak value 109 m^{-3} at 7.75 km. Ice crystals had similar height distribution as graupel but with maximum value 72 m^{-3}. Snowflakes were concentrated at 5.75–8.25 km with a maximum of 15 m^{-3}

at 7.25 km (Fig. 5b).

The higher mass density of graupel was between 6.75 km and 8.25 km, with a maximum of 15 mg m^{-3} at 6.75 km. Ice crystal mass density was one order lower than graupel, with maximum of 2 mg m^{-3}. The mass density distributions with height for both ice crystals and graupel were similar to their respective number density distribution in this case. The maximum mass density of frozen drops was 21.6 mg m^{-3} at 6.25 km. Super-cooled raindrops mass density was 10 mg m^{-3} above the 0°C level at 5.3 km (Fig. 5c).

2.2.4 *MIX5*

The cloud top had decreased to 10.5 km where temperature was −33.4°C, but radar reflectivity remained at 35 dBZ over Baoshan at 1611 BT 26 June when MIX5 was launched (Fig. 6a).

A total of 397 particles were observed by this sonde. Ice crystals had the highest number density, with a maximum of 86 m^{-3} at the −12°C level. At the same level, grauple density was 66 m^{-3}. Most ice crystals and graupel were concentrated between 5.5 km and 9 km in height. There were some snowflakes observed at 5.5 km and 11 km. The maximum diameter of the observed snowflakes was 3 mm. Super-cooled raindrops were observed between the levels of 0– -5°C, with maximum number density of 30 m^{-3} (Figs. 7a, b).

The mass density of grauple with a maximum of 12.5 mg m^{-3} at the −2°C level, was one order larger than that of ice crystals (1.11 mg m^{-3}). The mass density distributions for both ice crystals and graupel were different than their respective number density distributions, increasing with decreasing height below their peak number values at −10°C. Snowflakes reached a maximum mass density of 36.6 mg m^{-3} at 5.25 km, near the 0°C level. Frozen drops also existed near the 0°C level with mass density of 0.4 mg m^{-3} (Fig. 7c).

2.3 *Further observational analysis*

The satellite cloud pictures and radar echo displays show that well-developed convective cloud clusters were embedded in a wide Meiyu frontal cloud band. Therefore the Meiyu frontal cloud band was a mixed band: convective cloud embedded in stratiform cloud. Our videosondes mainly observed the overhead convective cloud.

Among the four sondes, rain was strongest during the first. Accordingly, UP11 discovered more particles, in both liquid and ice phases, than the other three sondes. The maximum number of ice crystals was often observed near the −10°C level. We may expect that a larger supersaturation for the ice phase, so favorable for the formation and deposition growth of ice crystals, occurred there. The distribution of mass density for ice crystals in three of the four sondes (UP9 excepted) was different from that of its number density: remaining steady or even increasing with decreasing height below its maximum number level. From this we may summerize expect that when ice crystals grew larger from deposition, they fell down and collected super-cooled cloud droplets and grew quickly. Observations from all four sondes show that the distribution patterns of both number and mass density for graupel were similar as those for ice crystals. So the formation of graupel must be related to ice crystals. The ice crystals could collect super-cooled cloud droplets and grow larger to become white opaque graupels. Also, the fact that the mass density of graupel mostly increased with decreasing height shows that graupel furthered its growth by collection with cloud and rain drops when it fell. The super-cooled raindrops existing near the 0°C level supported the further growth of the graupel via collision. The number density of graupel was generally less than, but mass density one order larger than the ice crystals. Therefore graupel and its collection with super-cooled drops played the most important role in the formation of rainfall. The numbers of snowflakes were fewer than the others, but the mass density was as large as that of graupel. So snowflakes were also important for the formation of rainfall. Near the 0°C level, there were quite large numbers of frozen drops. Now frozen drops are not easily broken when they collide with other droplets, so they could become larger and transform into large raindrops as they fall into the warm region and melt.

Below the 0°C level, liquid raindrops had a larger size and mass density. They were mainly from fallen and melted graupel, snowflakes, and frozen drops. In fact, some un-melted graupel was observed below the 0°C level. The mass density of raindrops somewhat increased with decreasing height which implies that larger raindrops might further grow from their coalescence with smaller raindrops when they fall.

From these analyses we may conclude:

(1) The ice-phase particles (ice crystals, graupel, and snowflakes) often existed in the cloud of torrential rain associated with the Meiyu front (although 4 sondes were presented in this paper, there was only one case among 14 sondes in which no ice-phase particle was observed). Ice crystals and graupel had the highest number density but graupel and snow had the highest mass density. Near the 0°C level, ice-phase particles (graupel, snowflakes, and also some frozen drops) coexisted with liquid water drops.

(2) The distribution of graupel was similar to that of ice crystals, so the collection of ice crystals with super-cooled droplets could be one of the main factors for graupel formation.

(3) The ice-phase particles grew larger by the collection with super-cooled cloud and rain droplets.

(4) Raindrops below the 0°C level were mainly generated from melted grauple, snowflakes and frozen drops. They may have further grown by coalescence with smaller drops as they fell from the cloud base.

3. Mesoscale numerical simulation

3.1 *Model description*

The non-hydrostatic model MM5 described by Grell et al. (1994) was used for numerical simulation. Three nested-level domains were set. The outer coarse domain included 61 × 61 grid points with horizontal resolution of 45 km; the same grid points for the middle domain but with 15 km grid size; the inner fine-mesh domain included 73 × 73 grid points with 5 km horizontal resolution. These covered the rainfall area near Shanghai for this case. The model atmosphere was divided into 25 layers from the surface to 50 hPa for all three domains. The version we used includes a high-resolution planetary boundary layer; Reisner graupel explicit moisture scheme for grid resolved precipitation physics in all three domains; and Anthes-Kuo, Grell, and none for cumulus convective parameterization schemes for grid non-resolved precipitation physics in the coarse, middle, and fine domains, respectively. The model was initiated using the USA NCEP grid data as a "first guess" field, supplemented by China National Meteorological Center operational surface and rawinsonde data. The time-dependent inflow-outflow conditions were used for the lateral boundary. The model simulation was started at 0800 BT 25 June and ended at 2000 BT 26 June 1999. Real terrain data with resolutions of 30 min., 10 min, and 5 min. were used for the three domains, respectively. Simulations were shown by using the 5-D visual system to see the distribution and evolution of various hydrometeors.

3.2 *Comparison between simulations and observations*

For testing the simulations, the prognostic contour charts and wind fields on low , mid-, and high-levels; vertical cross sections of equivalent potential temperature, radar reflectivity, cloud top height and temperature; total 12 h, 24 h, and 36 h rainfall, and rainfall variation in 6 h intervals from observations and simulations were compared.

3.2.1 *Prognostic contour chart, wind field, and equivalent potential temperature*

The model well simulated the subtropical high and its westward movement on the 500 hPa isobaric surface, high level jet at 200 hPa, and the surface low near the Meiyu front along the Yangtze river. The southwest jet at the low level (850 hPa) was well simulated over the 24 hours but had a bias towards the north of about 2 4° of latitude. Both the analysis and simulation of the vertical cross section of equivalent potential temperature through the Meiyu front show a dense belt, and its south edge near 30°N was the position of the surface Meiyu front (figures omitted).

3.2.2 *Radar reflectivity*

Radar reflectivity from the simulation was calculated from $\mathrm{dB}Z=\mathrm{dB}Z_\mathrm{r}+\mathrm{dB}Z_\mathrm{i}$ where $\mathrm{dB}Z_\mathrm{r}$ and $\mathrm{dB}Z_\mathrm{i}$ represents the contribution from rain- and ice-phase drops, respectively. According to Herzegh and Hobbs (1980), $\mathrm{dB}Z_\mathrm{r}=42.2+16.8\log M_\mathrm{r}$, and $\mathrm{dB}Z_\mathrm{i}=41.4+16.5\log(M_\mathrm{i}+M_\mathrm{s}+M_\mathrm{g})$, where $M_\mathrm{r}=10^3\rho q_\mathrm{r}$, $M_\mathrm{i}=10^3\rho q_\mathrm{i}$, $M_\mathrm{s}=10^3\rho q_\mathrm{s}$, and $M_g=10^3\rho q_\mathrm{g}$. The variables q_r, q_i, q_s, and q_g are mixing ratio of rain water, ice crystals, snow, and grauples, respectively, and ρ is the density of dry air.

The simulated reflectivity of 40 dBZ at 600 hPa ($\sim$ 4.5 km) at 33 h integration (valid for 1700 BT 26 June) was consistent with the observed 35 dBZ at 4.5 km height over Baoshan at 1600 BT 26 June (Fig. 6). Also both observation and simulation show the radar echo top was at 10 km of height.

3.2.3 *Cloud top temperature and satellite brightness temperature*

The simulated cloud top was estimated by $q_\mathrm{c}+q_\mathrm{r}+q_\mathrm{i}+q_\mathrm{s}+q_\mathrm{g}\geq 0.01$ g kg^{-1} (Liu and Zhang, 1997). The temperature of the cloud top was compared with the satellite brightness temperature TBB. Figure 8 shows the TBB distribution of satellite observation at 0800 BT 26 June and model 24 h simulation valid for the same time. It shows that they are generally similar: convective cloud clusters were embedded in a southwest to northeast distributed cloud band, and the temperature of the cloud top was as low as $-$ $-$ 50°C in Hangzhou area (near 30°N, 115°E). The evolution of the simulated cloud top temperature distribution was also similar with that of the TBB observations.

3.2.4 *Rainfall*

Figure 9 shows the 36 h accumulated rainfall from observation and simulation. The major part of the rainband was simulated very well except the west edge of the band. A false rainfall maximum appeared at 31°N, 115°E in the simulation pattern, which was caused by the grid non-resolved cumulus convective rain treated by cumulus parameterization. This was verified by Fig. 10 which shows total 36 h rainfall of grid resolved rainfall from the Reisner explicit scheme and grid non-resolved rainfall from the cumulus parameterization scheme, respectively. We could see the pattern of rainfall treated by the explicit scheme (Figs. 10a) fit the observation well, and the unmatched part to the west of the rainband was caused by the cumulus parameterization (Fig. 10b).

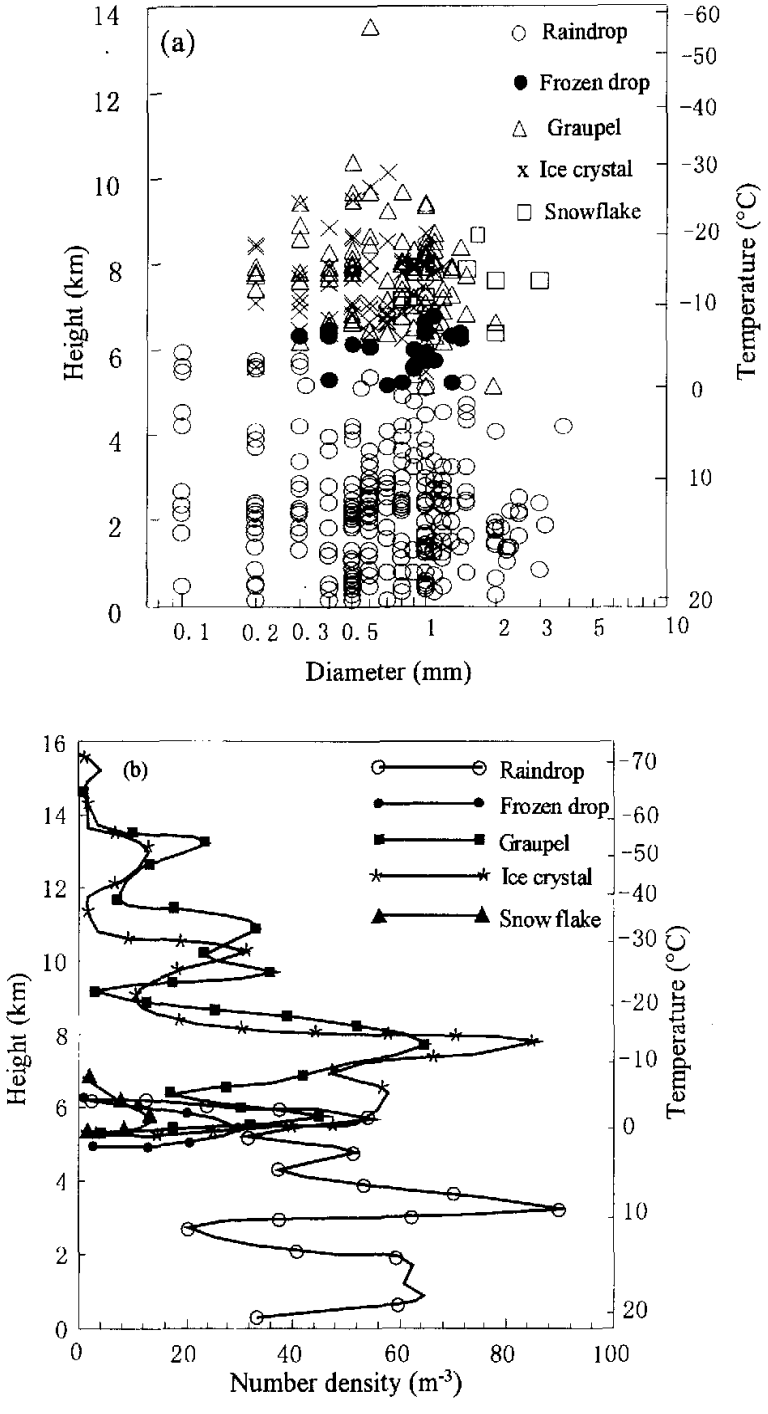

Fig. 7. Same as Fig. 3 but for MIX5.

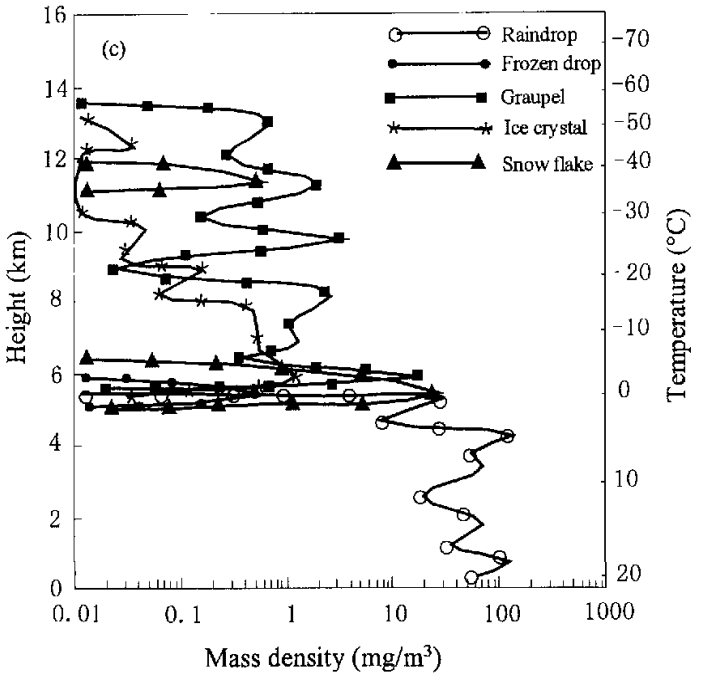

Fig. 7. (Continued)

The above comparison shows that the model simulations well represented the observations, and the cloud physical processes treated by the Reisner scheme reasonably represented those in the cloud for this case. Thus, we can use the model-retrieved data to analyze the cloud physical processes and their evolution.

In the Reisner graupel explicit scheme, mixing ratios of cloud water, rain water, ice, snow, and graupel are prognostic variables. The equations for the mixing ratios of water vapor q_v, cloud water q_c, rain water q_r, cloud ice q_i, snow q_s, and graupel q_g are the following.

3.3 *Cloud physical process simulation*

$$\frac{\partial p^* q_v}{\partial t} = -\mathrm{ADV}(p^* q_v) + \mathrm{DIV}(p^* q_v) + \mathrm{D}(q_v) + p^*(P_{revp} - P_{idep} - P_{sdep} - P_{gdep} - P_{idsn} - P_{ccnd}),$$

$$\frac{\partial p^* q_c}{\partial t} = -\mathrm{ADV}(p^* q_c) + \mathrm{DIV}(p^* q_c) + \mathrm{D}(q_c) + p^*(-P_{ccnr} - P_{racw} + P_{ccnd} - P_{ifzc} - P_{ispl} - P_{s.sacw} - P_{g.sacw} - P_{gacw} - P_{i.iacw} - P_{g.iacw} + P_{imlt}),$$

$$\frac{\partial p^* q_r}{\partial t} = -\mathrm{ADV}(p^* q_r) + \mathrm{DIV}(p^* q_r) - P_{rprc} + p^*(P_{racw} + P_{ccnr} - P_{revp} - P_{gfzr} - P_{iacr} - P_{s.sacr} - P_{g.sacr} - P_{gacr} + P_{smlt} + P_{gmlt}),$$

$$\frac{\partial p^* q_i}{\partial t} = -\mathrm{ADV}(p^* q_i) + \mathrm{DIV}(p^* q_i) + \mathrm{D}(q_i) + p^*(P_{idsn} + P_{ifzc} + P_{ispl} + P_{idep} + P_{i.iacw} - P_{icng} - P_{raci} - P_{saci} - P_{icns} - P_{imlt}),$$

$$\frac{\partial p^* q_s}{\partial t} = -\mathrm{ADV}(p^* q_s) + \mathrm{DIV}(p^* q_s) - P_{sprc} + p^*(P_{sdep} + P_{icns} + P_{s.sacw} - P_{scng} + P_{saci} + P_{s.sacr} - P_{g.racs} - P_{smlt}),$$

$$\frac{\partial p^* q_g}{\partial t} = -\mathrm{ADV}(p^* q_g) + \mathrm{DIV}(p^* q_g) - P_{gprc} + p^*(P_{gdep} + P_{scng} + P_{g.sacw} + P_{gacw} + P_{gacr} + P_{iacr} + P_{raci} + P_{g.sacr} + P_{g.racs} + P_{gfzr} + P_{icng} + P_{g.iacw} - P_{gmlt}).$$

Here p^* is the difference between the surface pressure and the pressure at the top, D represents diffusion due to sub-grid scale turbulence. The ADV and DIV terms represent three-dimensional advection and divergence. The P_{xxxx} terms on the right-hand side of the equations are the various source and sink terms for the generation of hydrometeors (Reisner et al., 1998).

3.3.1 *Distribution and evolution of mixing ratios of cloud water, rain water, cloud ice, snow and graupel*

(1) Cloud water

Observations from satellite and radar have shown that the Meiyu frontal precipitation band was often embedded by meso-β and meso-γ scale cloud clusters which caused heavy rainfall on the surface (e.g., Xu et al., 2000). Our simulations show cloud water was distributed into a stratiform cloud band in which convective cloud clusters were embedded (Fig. 11a). The cloud clusters had a horizontal scale of 10^0–10^1 km, their top reached up to 8 km, and the mixing ratio of the cloud water was 0.2–0.5 g kg^{-1}. Since the 0°C level was at 5.5 km height, the cloud water above 5.5 km was in a super-cooled state. Each cloud cluster experienced its life cycle of developing, maturing, and dissipating in several to twenty hours. Two or more cloud clusters might combine together into a larger one and remain longer.

(2) Ice water

Ice water was also distributed into a southwest to northeast band (Fig. 14b). Its mixing ratio was 10^{-5} 10^{-3} g kg^{-1}, two to four orders less than that of cloud water. It was concentrated at the upper part of the cloud between 8 16 km.

(3) Snow

Snow was distributed from 4 km to 12 km in height, with a maximum value of 1.4 g kg^{-1} near the 0°C level (Fig. 11c).

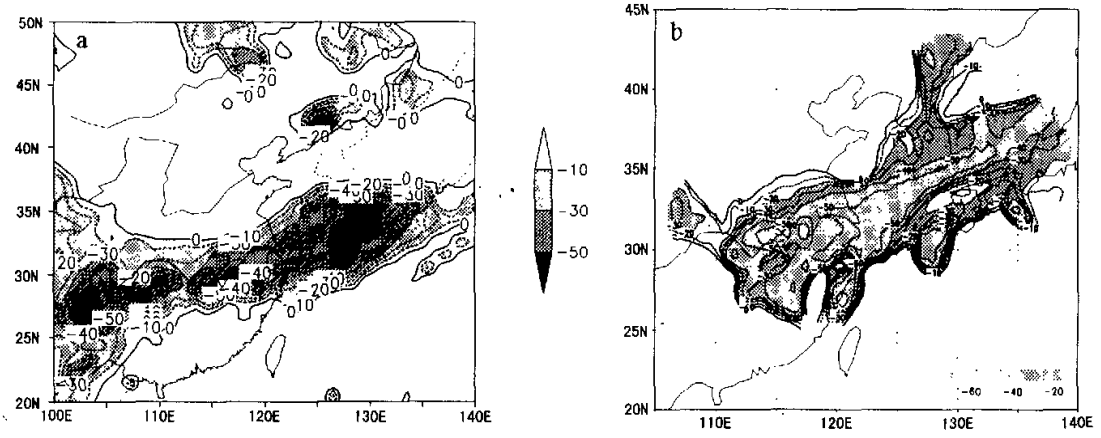

Fig. 8. (a) TBB from GMS satellite observation at 0800 BT 26 June 1999. (b) TBB from model simulation 24 h integration and valid for 0800 26 June 1999.

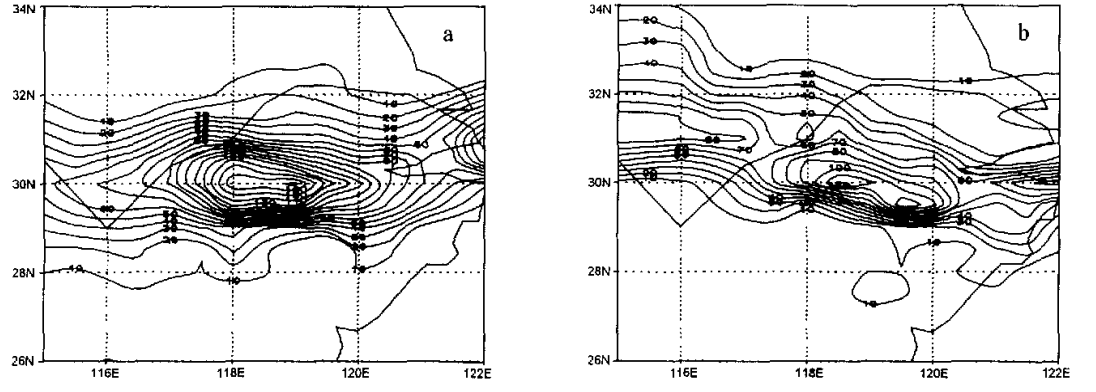

Fig. 9. Accumulated rainfall from observations (a) and simulations (b) at 36 h (in mm).

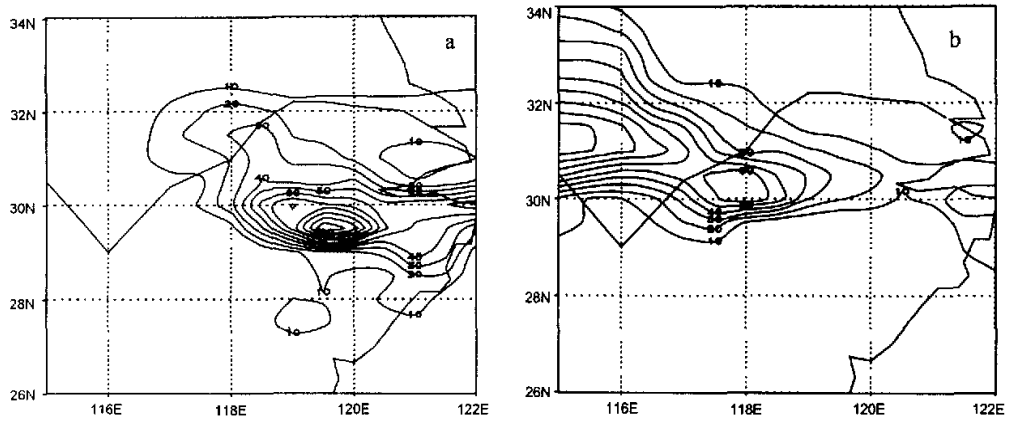

Fig. 10. Model-simulated accumulated rainfall contributed from grid resolved rain (a) and grid non-resolved rain (b) at 36 h.

(4) Graupel

Graupel was distributed from 4 km to 10 km in height with a maximum value of 2.2 2.4 g kg^{-1} near the 0°C level (Fig. 11d).

(5) Rain water

Rain water was mostly distributed in the warm part of the cloud with a maximum of 1–2.0 g kg^{-1}. Comparing Fig. 11e with Figs. 11c and 11d we can see its distribution and evolution corresponded well to that of the ice-phases (include snow and graupel), i.e. the rain water maximum, and also for surface rainfall shown in Fig. 11f, was located just under the ice-phase maximum, and was developing and dissipating with the ice-phase simultaneously.

3.3.2 *Comparison with videosonde observations*

The videosonde observations UP9 and MIX5 on 26 June 1999 correspord to 21 h and 33 h integration of the simulation. For comparing with the observations, mass density of cloud water, cloud ice, snow, graupel, and rain water were calculated from $M_p = \rho q_p$, where q_p is the mixing ratio of the hydrometeors and ρ is dry air density. Vertical cross sections of mass density of ice, snow, graupel, and rain through Baoshan (located at 31.5°N, 121.5°E) are shown in Fig. 12. In the cross section, Baoshan is between 40 and 41 at the x-axis.

In Fig. 12 integration at 21 h (valid for 0500 BT 26 June) shows that ice water was spread from 8–16 km with a maximum of 5 mg m^{-3} at 11 km; snow from 4–11 km with a maximum of 250 mg m^{-3} at 5 km; graupel from 4–7 km with a maximum of 4 mg m^{-3} at 5 km; and rain water was below 5.5 km with a maximum of 100 mg m^{-3} at 3.5 km (Figs. 12a, b, c, d). Observations by UP9 between 0440–0540 BT 26 June show ice crystals spread from 6–10 km with a maximum of 2 mg m^{-3} at 8 km; snow flakes from 5–8 km with a maximum of 10 mg m^{-3} at 8 km; graupel from 5–10 km with a maximum of 10 mg m^{-3} at 7 km; and raindrops below 6 km with a maximum of 200 mg m^{-3} at 2 km (Fig. 5c), Comparing the two groups of data, we can see that they show distributions at similar height levels with the same orders of maximum except for cloud ice. The PPIS observed that most ice crystals were at lower levels than given by the simulations. The PPIS observation might miss small ice crystals at upper levels where no particles larger than 0.5 mm in diameter might exist, and hence could not trigger the flash of light.

Table 1 Comparison between model simulations and video sounding observations of mass density for various water species

	21 h (0500 26 June)		UP9 (0440-0540 26 June)		33 h (1700 26 June)		MIX5 (1611–1700 26th June)	
Ice water	8–16 km	5 mg m^{-3} 11 km	6–10 km	2 mg m^{-3} 8 km	8–16 km	4 mg m^{-3} 11–12 km	5–13 km	1 mg m^{-3} 6 km
Snow	4–11 km	250 mg m^{-3} 5 km	5–8 km	10 mg m^{-3} 8 km	4–12 km	240 mg m^{-3} 5.5 km	5–12 km	36 mg m^{-3} 5 km
Graupel	4–7 km	4 mg m^{-3} 5 km	5–10 km	10 mg m^{-3} 7 km	4–7 km	8 mg m^{-3} 5 km	5–13 km	12 mg m^{-3} 6 km
Rain water	< 5.5 km	100 mg m^{-3} 3.5 km	< 6 km	200 mg m^{-3} 2 km	< 5.5 km	130 mg m^{-3} 3 km	< 5.5 km	100 mg m^{-3} 4 km

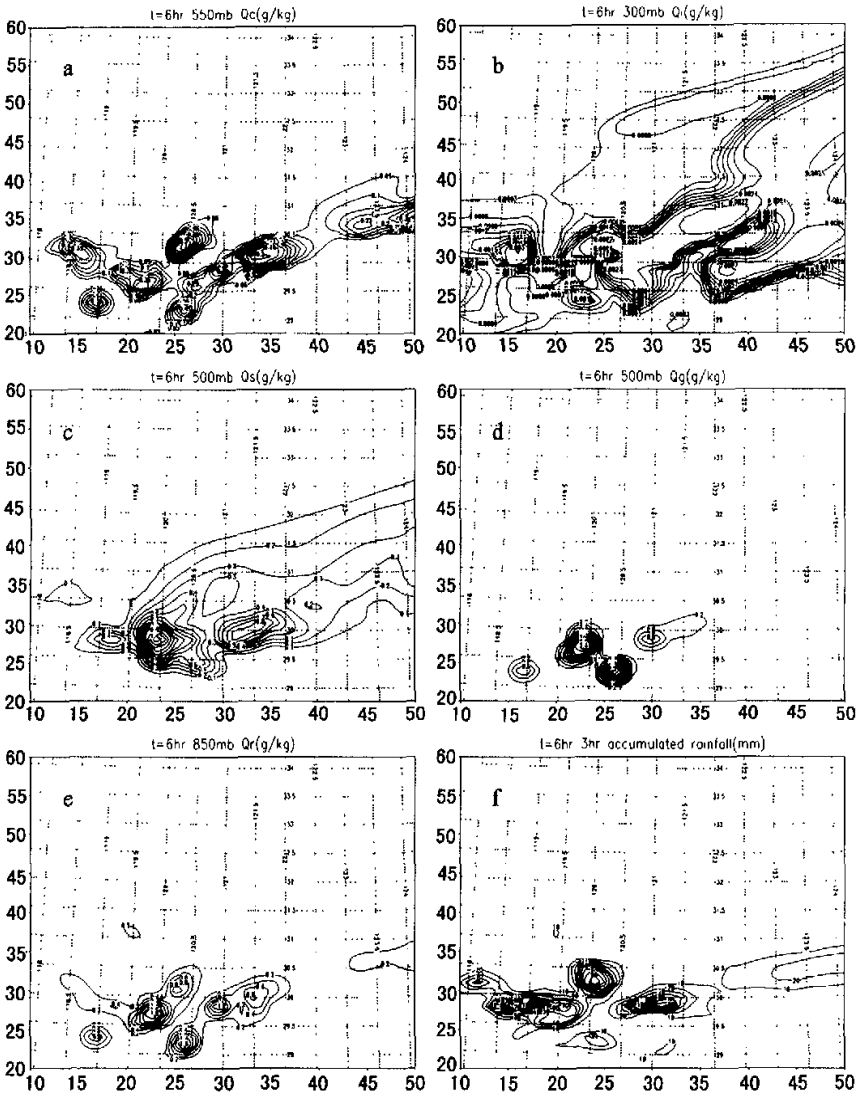

Fig. 11. Simulation at 6 h integration of (a) cloud water on isobaric surface 550 hPa, (b) cloud ice on 300 hPa, (c) snow on 500 hPa, (d) graupel on 500 hPa, (e) rain water on 850 hPa, (f) surface accumulated rainfall in 3 hours. Labeled in g kg^{-1} for cloud water, cloud ice, snow, graupel, and rain water, and in mm for surface rainfall.

Comparing model integration at 33 h (Figs. 12e, f, g, h) with videosonde MIX5 observations (Fig. 7c) shows similar results. Table 1 lists these comparisons.

3.3.3 *Sources and sinks*

The major sources and sinks for the generation of cloud water, cloud ice, snow, graupel and rain water are considered to see the major contributing factors. Here only those simulated at 21 h integration and valid for 0500 26 June when rain intensity was increasing and PPIS UP9 was launching are given below as an example.

The major source for cloud ice generation was riming growth ($P_{\text{i.iacw}}$), with a maximum of 2×10^{-7} g $kg^{-1}s^{-1}$ at 400 hPa. The ice multiplication (P_{ispl}) was the next main factor for its generation, with a

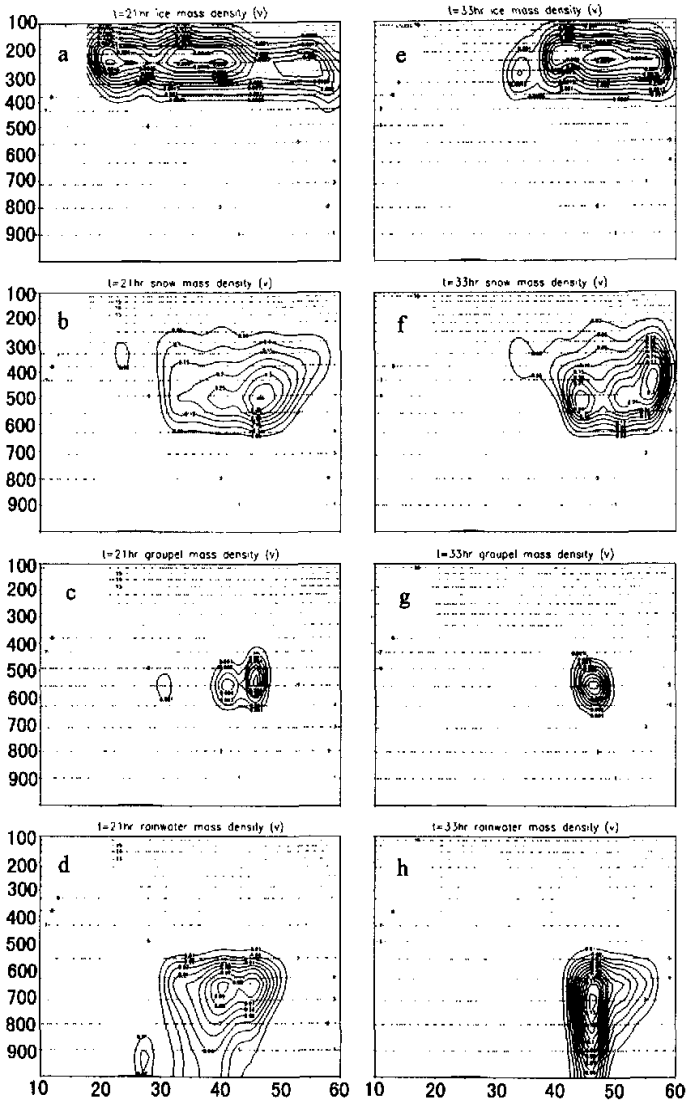

Fig. 12. Vertical cross section of mass density of ice, snow, graupel, and rain water labeled in g m^{-3} along 121.5°E from 21 h and 33 h integration of model simulation valid for 0500 BT 26 and 1700 26 June, respectively. In figures, the numbers on horizontal lines represent height in km.

maximum of 3×10^{-10} g $kg^{-1}s^{-1}$ near 500 hPa. The contribution from freezing of cloud droplets was less than the others, with a maximum of 1.6×10^{-11} g $kg^{-1}s^{-1}$.

For snow, the deposition (P_{sdep}), with a maximum of 1.0×10^{-4} g $kg^{-1}s^{-1}$, played an important role in the upper part of the cloud. When snow particles grew and fell to the lower part of the cloud (below 500 hPa), the collection of rain water by snow ($P_{s.sacr}$) became the major factor, (maximum 5.5×10^{-4} g $kg^{-1}s^{-1}$). Simulations show that ice collection with snow (P_{saci}) and ice conversion into snow (P_{icns}) were not important; both of them were less than 2×10^{-7} g $kg^{-1}s^{-1}$. Therefore the existence of super-cooled cloud and rain water was important for the growth of snowflakes.

Table 2 lists the main sources and sinks for the

major water hydrometeors.

Table 2 Main sources and sinks for generation of ice, snow, graupel, and rain water simulation at 21 h valid for 0500 BT 26 June

Category of water species	Main sources and sinks (numbers in the brackets are the maximum with units of g kg $^{-1}$s $^{-1}$)
Cloud ice	$P_{\text{i.iacw}}(2 \times 10^{-7})$, $P_{\text{ispl}}(3 \times 10^{-10})$, $P_{\text{ifzc}}(1.6 \times 10^{-11})$
Snow	$P_{\text{s.sacr}}(5.5 \times 10^{-4})$, $P_{\text{sdep}}(1 \times 10^{-4})$, $P_{\text{saci}}(\leq 2 \times 10^{-7})$, $P_{\text{icns}}(\leq 2 \times 10^{-7})$
Graupel	$P_{\text{g.racs}}(6 \times 10^{-4})$, $P_{\text{g.sacr}}(5.5 \times 10^{-4})$, $P_{\text{gacr}}(2.2 \times 10^{-4})$, $P_{\text{gacw}}(7 \times 10^{-6})$, $P_{\text{g.sacw}}(3.3 \times 10^{-6})$, $P_{\text{g.iacw}}(1.1 \times 10^{-6})$
Rain water	$P_{\text{smlt}}(8 \times 10^{-5})$, $P_{\text{gmlt}}(9 \times 10^{-6})$, $P_{\text{racw}}(5 \times 10^{-9})$, $P_{\text{ccnr}}(6 \times 10^{-10})$

For graupel, conversion from collection of rain by snow ($P_{\text{g.racs}}$), or vice versa, from collection of snow by rain ($P_{\text{g.sacr}}$), played the most important role. The maximum of $P_{\text{g.sacr}}$ was 6×10^{-4} and of $P_{\text{g.racs}}$ 5.5×10^{-4} near the 5 km level (0°C level). Therefore, the formation of snow and co-existence with rain water were favorable for the formation and growth of graupel. Graupel could grow further by collection with cloud water (P_{gacw}) and rain water (P_{gacr}), whose maximums were 2.2×10^{-4} g kg^{-1}s^{-1} and 7×10^{-6} g kg^{-1}s^{-1}, respectively. Other generation terms for the formation of graupel were snow accretion of cloud water ($P_{\text{g.sacw}}$), with a maximum of 3.3×10^{-6} g kg^{-1}s^{-1}, and collection of cloud water by ice ($P_{\text{g.iacw}}$), maximum of 1.1×10^{-6} g kg^{-1}s^{-1}. Snow accretion of cloud water and collection of cloud water by ice then converted into graupel ($P_{\text{g.sacw}}$, $P_{\text{g.iacw}}$) were also important for the formation and growth of graupel, 3.3×10^{-6} g kg^{-1}s^{-1} and 1.1×10^{-6} g kg^{-1}s^{-1}, respectively. Freezing of rain water into graupel (P_{gfzr}) and collection of ice by rain (P_{raci}) were small and not important.

For rain water, the source terms include generation due to the collection of cloud water by rain (P_{racw}), conversion of cloud water into rain (P_{ccnr}), and melting of snow (P_{smlt}) and graupel (P_{gmlt}). Simulations show the melting of snow (P_{smlt}, 8×10^{-5} g kg^{-1}s^{-1})and graupel (P_{gmlt}, 9×10^{-6} g kg^{-1}s^{-1}) were the most important factors for rain water generation at the low level, and the other two factors (P_{racw}, 5×10^{-9} g kg^{-1}s^{-1} and P_{ccnr}, 6×10^{-10} g kg^{-1}s^{-1}) were 3–4 orders of magnitude less than them.

Running the model with a "warm cloud scheme", in which the similar mechanism for the generation of cloud water and rain as that in the Reisner scheme is used but the ice phase excluded, shows that the accumulated 12, 24, and 36 h rainfall was only 60% of that with the Reisner scheme. This verifies, in another way, that the ice phase and its interaction with the liquid phase in cloud, i.e. the mixed-phase cloud physical process, is the major important process for the formation and development of heavy rainfall associated with the Meiyu front.

4. Conclusion

In analyzing this heavy rainfall event, it was found that the synoptic scale Meiyu frontal cloud and rainband was generally embedded with meso-scale convective cloud and rain clusters which mainly contributed to heavy rainfall on the surface.

Videosonde observations and analyses for the convective cloud and rain clusters show that ice-phase particles (ice crystals, graupel, snowflakes, and frozen drops) mostly existed in the cloud. Among these particles, ice crystals and graupel were the most numerous but graupel and snow had the highest mass density. Near the 0°C level, ice-phase particles coexisted with liquid water droplets. The fact that the distribution with height of graupel was similar to that of ice crystals implies that the collection of ice crystals with super-cooled cloud and rain droplets could be one of main factors for graupel formation and growth. Raindrops below the 0 °C level were mainly produced by falling from above and melted grauple, snowflakes, and frozen drops.

Numerical simulations using the non-hydrostatic meso-scale model MM5 with the Reisner explicit scheme mainly verified the results from observations except for the cloud ice distribution with height. The ice crystals were distributed lower in the observations than in the model simulations, which may be caused by the deficiencies of PPIS observation for small particles. The analyses of sources and sinks for various hydrometeors from simulation show that rain water below the cloud base, and so for surface rainfall, were mainly from snow and graupel melting. The growth of snow and graupel in the cloud was mainly from collection with cloud and rain water near 0°C. Hence the distribution and evolution of rain water on the low level, and so for surface rainfall, corresponded well with those of snow and graupel on the upper level.

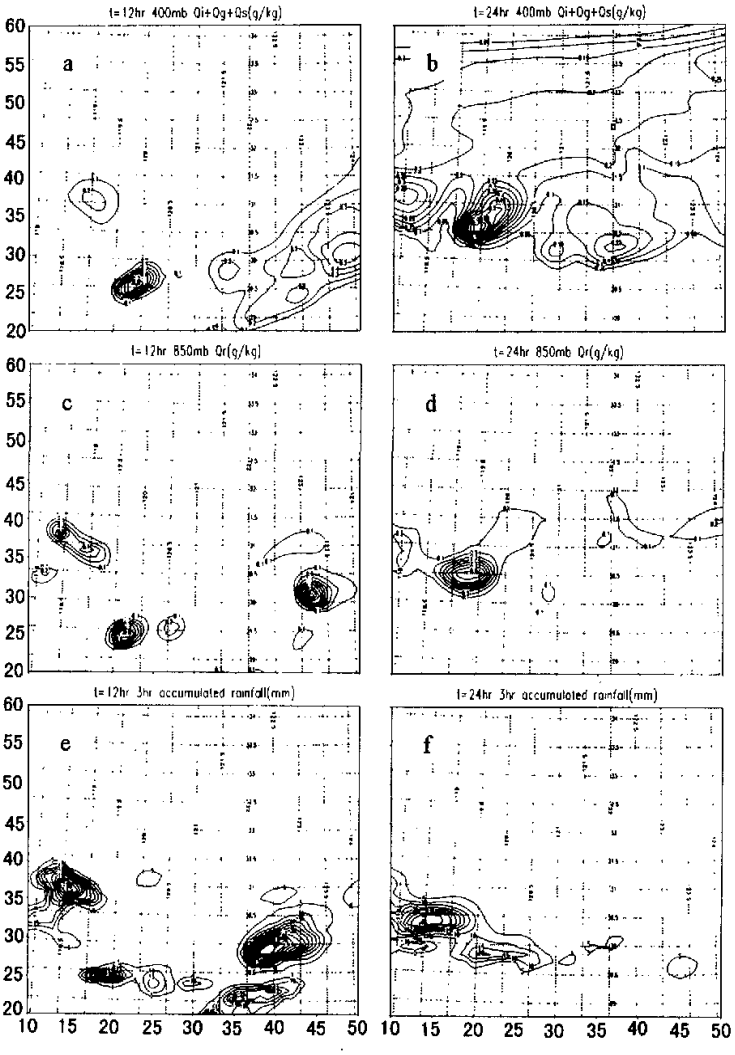

Fig. 13. Simulated ice-phase water (ice, snow, and graupel) on 400 hPa level (a, b), rain water on 850 hPa (c, d), and surface accumulated rainfall in 3 hours (e, f) at 12 h and 24 h integration.

Thus, the mixed-phase cloud process, in which ice phase (ice, snow, graupel) coexisted with liquid phase (cloud water and rain), played the most important role in the formation and development of heavy convective rainfall in the Meiyu frontal system. This finding was similar to the one in the case of the South China heavy rainfall discussed by Wang et al. (2002).

Acknowledgments. This study was supported by the State Key Basic Program: Research on the Formation Mechanism and Prediction Theory of Severe Synoptic Disasters in China No.G1998040907 and the National Natural Sciences Foundation of China under Grant No. 49735180. The videosonde observations at Baoshan in 1999 were done in cooperation with Prof. Tsutomu Takahashi (Obirin University, Japan). We thank Prof. T. Takahashi and Prof. Xu Baoxiang for successfully organizing the observations. We also thank the Shanghai Meteorological Bureau and Mr. Yang Shaozhong for assisting with the data collection.

REFERENCES

Chen S. J., 1989: Numerical study on the coupling of high-low level circulation in the process of heavy rainfall in later Meiyu period. *Acta. Meteor. Sinica*, **47**, 8–15. (in Chinese)

Cheng M. H. He H. Z., Mao D. Y., Qi Y. J., Cui Z. H., and Zhou F. X., 2001: Study of 1998 heavy rainfall over the Yangtze river basin using TRMM data. *Advances in Atmospheric Sciences*, **18**, 387–396.

Grell, G. A., J. Dudhia, and D. R. Stauffer, 1994: A description of the fifth generation Penn State/NCAR mesoscale model (MM5). NCAR/TN-398+STR NCAR technical note., 138pp.

Herzegh, P. H., and P. V. Hobbs, 1980: The mesosclae and microscale structure and organization of clouds and precipitation in mid-latitude cyclones. Part II: Warm front clouds. *J. Atmos. Sci.*, **37**, 597–611.

Li S. L., Ji L. R., Lin W. T., and Ni Y. Q., 2001: The maintenance of the blocking over the Ural mountains during the second Meiyu period in the summer of 1998. *Advances in Atmospheric Sciences*, **18**, 87–105.

Liu Y. B., and D. L. Zhang., 1997: A multiscale numerical study of hurricane Andrew (1992). Part I: Explicit simulation and verification. *Mon. Wea. Rev.*, **125**, 3073 3093.

Reisner, J., R. M. Rasmussen, and R. T. Bruintjes, 1998: Explicit forecasting of supercooled liquid water in winter storms using the MM5 model. *Quart. J. Roy. Meteor. Soc.*, **124**, 1071–1107.

Takahashi, T., K. Suzuki, and M. Orita, 1995: Videosonde observation of precipitation processes in equatorial cloud clusters. *J. Meteor. Soc. Japan*, **73**, 509–534.

Xu H., Zhang W. P., Lang X. X., Guo X., Ge W. Z., Dang R. Q., and T. Takeda, 2000: The use of dual-doppler radar in the study of 1998 Meiyu frontal precipitation in Huaihe river basin. *Advances in Atmospheric Sciences*, **17**, 403–412.

Xue Q. F., Liu J. L., and Ding Y. H., 1996: The interactions of synoptic and subsynoptic scale system in a heavy rain process. *Mesoscale Synoptic and Dynamic Research*. China Meteorological Press, 35–41 (in Chinese).

Yu Z. H., and Lu H. C., 1988: Mesoscale rainband and rain clusters of Meiyu front. *Scientia Sinica* (*B*), **9**, 1002–1010 (in Chinese).

Wang P. Y., Ruan Z., and Kang H. W., 2002: Numerical study on cloud physical processes of heavy rainfall of South China. *J. Appl. Meteor. Sci.*, **13**, 78 87 (in Chinese).

Zhai G. Q., and Gao K., 1996: The simulation study of the effects of upper stream surface thermal fluxes on Changjiang Huaihe river basin cyclone accompanied with heavy rain. *Mesoscale Synoptic and Dynamic Research*, China Meteorological Press, 282 293 (in Chinese).

梅雨锋暴雨中云物理过程的观测和数值模拟

王鹏云 杨 静

摘 要

1999年6 7月在上海对梅雨锋暴雨中云物理结构进行了摄像探空观测。观测给出云中各种降水粒子的大小、数浓度和质量浓度的垂直分布。在多数对流性云雨团中都观测到冰相降水元（冰晶，雪，霰，冻滴）。其中，数浓度以冰晶和霰最大，质量浓度以霰和雪最大。在零度层附近为冰相和液相（云、雨滴）混存区。霰的质量浓度随高度降低而增加。在零度层以下暖区观测到尚未融化完的霰和雪片。用MM5所作的中尺度数值模拟研究表明，梅雨锋雨带对流性云团中，雨水和地面降水与云中冰相降水元的发展、演变和移动相一致。对云中各种水成物的源、汇项分析表明，零度层下方雨水主要由高层落下的雪晶和霰融化而成，霰和雪则主要由其在冷区与过冷云雨水碰冻长大。与摄像探空观测结果比较，降水元分布与观测结果基本一致。因而，冰水相共存和相互作用是形成梅雨暴雨的主要云物理过程

关键词：梅雨锋暴雨，云物理，摄像探空，中尺度数值模拟